Chemical Science

ROYAL SOCIETY OF CHEMISTRY

EDGE ARTICLE

View Article Online
View Journal | View Issue

Cite this: *Chem. Sci.*, 2026, **17**, 1721

All publication charges for this article have been paid for by the Royal Society of Chemistry

Received 17th September 2025
Accepted 24th November 2025

DOI: 10.1039/d5sc07181j

rsc.li/chemical-science

Phosphorescent iridium complexes activated by endogenous zinc as a mitochondrial DNA nuclease for stimulation of the cGAS-STING pathway

Zhi-Yuan Li,†[ac] Long-Bo Yu,†[ac] Qing-Hua Shen,[ac] Liang Hao,[abc] Peng Wang,[ac] Xiao-Xiao Chen,[ac] Yu-Yi Ling*[abc] and Cai-Ping Tan *[acd]

Zinc is a crucial element in cellular processes, and its homeostasis has intricate relationships with the initiation, progression, and therapeutic intervention of cancer. Activation of the cyclic GMP-AMP synthase (cGAS)-stimulator of interferon genes (STING) pathway has been proven to be an effective strategy for cancer immunotherapy. Herein, we report four phosphorescent iridium complexes (**Ir1–Ir4**) with zinc chelating ligands. Among them, **Ir1** can bind and image mitochondrial chelatable zinc ions *via* phosphorescence-lifetime responses, consequently modulating the expression of zinc-regulatory proteins. Furthermore, the *in situ* formed heteronuclear metal complex **Ir1-Zn$_2$** shows nuclease mimetic activities, capable of hydrolyzing mitochondrial DNA (mtDNA) to release mtDNA fragments for the activation of the cGAS-STING pathway. In conclusion, we designed a mitochondria-targeting phosphorescent Ir(III) complex with dual functions in dysregulation of zinc homeostasis and generation of nuclease *in situ*, which provides an innovative approach to stimulate the cGAS-STING pathway.

Introduction

Cyclic GMP-AMP synthase (cGAS) is an intracellular sensing molecule that can recognize DNA within cells, usually originating from pathogens, and activates the stimulator of interferon genes (STING) pathway, thereby triggering antitumor immune responses.[1,2] The cGAS-STING pathway holds significant promise in cancer treatment, especially in enhancing the immune response and advancing combination immunotherapy.[3,4] However, further research and clinical trials are essential to fully harness its potential in cancer treatment.[5,6] Specifically, the development of small-molecule activators of the cGAS-STING pathway is still very limited.[7] Cyclic dinucleotides (CDNs) and their analogs, such as ADU-S100 (ref. 8) and MK-1454,[9,10] have entered clinical trials. A series of non-nucleotide small-molecule STING agonists, such as diABZI and its derivatives,[11,12] MSA-2,[13] SR-717,[14] NVS-STG2,[15] and PDIC-NS[16] as well as multivalent polymers like PC7A,[17,18] were reported to be effective activators of the cGAS-STING pathway. Diverse nanomaterials, *e.g.*, inorganic nanomaterials, organic polymeric materials, lipid-based nanomaterials, and biomimetic nanomaterials have been developed for the encapsulation and delivery of CDNs or STING agonists.[19–23] Specifically, intracellular metal ions, *e.g.*, Mn^{2+} (ref. 24) and Zn^{2+},[25,26] have demonstrated regulatory effects on the cGAS-STING pathway. Additionally, metal complexes, such as platinum,[27–31] rhodium,[32] iridium,[33,34] ruthenium,[35,36] manganese,[37] gold,[38] and osmium complexes,[39] have shown potential in STING activation. Moreover, the combination therapy of STING agonists with immune checkpoint inhibitors (ICIs) has been proven to further enhance anti-tumor immune responses.[40–43]

As the second most abundant transition metal element in the human body, zinc not only acts as a cellular signaling mediator to regulate signaling pathways and enzyme activities, but also participates in the regulation of cellular ionic homeostasis and biomolecule metabolism as protein components and enzyme cofactors.[44,45] The intracellular concentration of labile zinc ranges from pM to nM,[46] and the cellular zinc homeostasis is regulated by complex mechanisms. Important components of this regulation include zinc finger proteins, superoxide dismutase (SOD) and metal-responsive element-binding transcription factor (MTF)-1, and the zinc transporter proteins, including Zrt/Irt-like protein (ZIP, SLC39A) family, Zn^{2+} transporter protein (ZnTs, SLC30A) family, and metallothioneins (MTs).[47–49] Zn^{2+} has been found to function in various physiological processes, including neuronal transmission and cancer immunity.[25] Dysregulation of zinc homeostasis is closely

[a]*MOE Key Laboratory of Bioinorganic and Synthetic Chemistry, School of Chemistry, Sun Yat-Sen University, Guangzhou 510006, China. E-mail: lingyy@gdmu.edu.cn; tancaip@mail.sysu.edu.cn*

[b]*The Marine Biomedical Research Institute of Guangdong Zhanjiang, School of Ocean and Tropical-Medicine, Guangdong Medical University, Zhanjiang, Guangdong, 524023, China*

[c]*Guangdong Basic Research Center of Excellence for Functional Molecular Engineering, Guangzhou 510006, China*

[d]*State Key Laboratory of Anti-Infective Drug Discovery and Development, School of Pharmaceutical Sciences, Sun Yat-sen University, Guangzhou 510006, China*

† These authors contributed equally to this work.

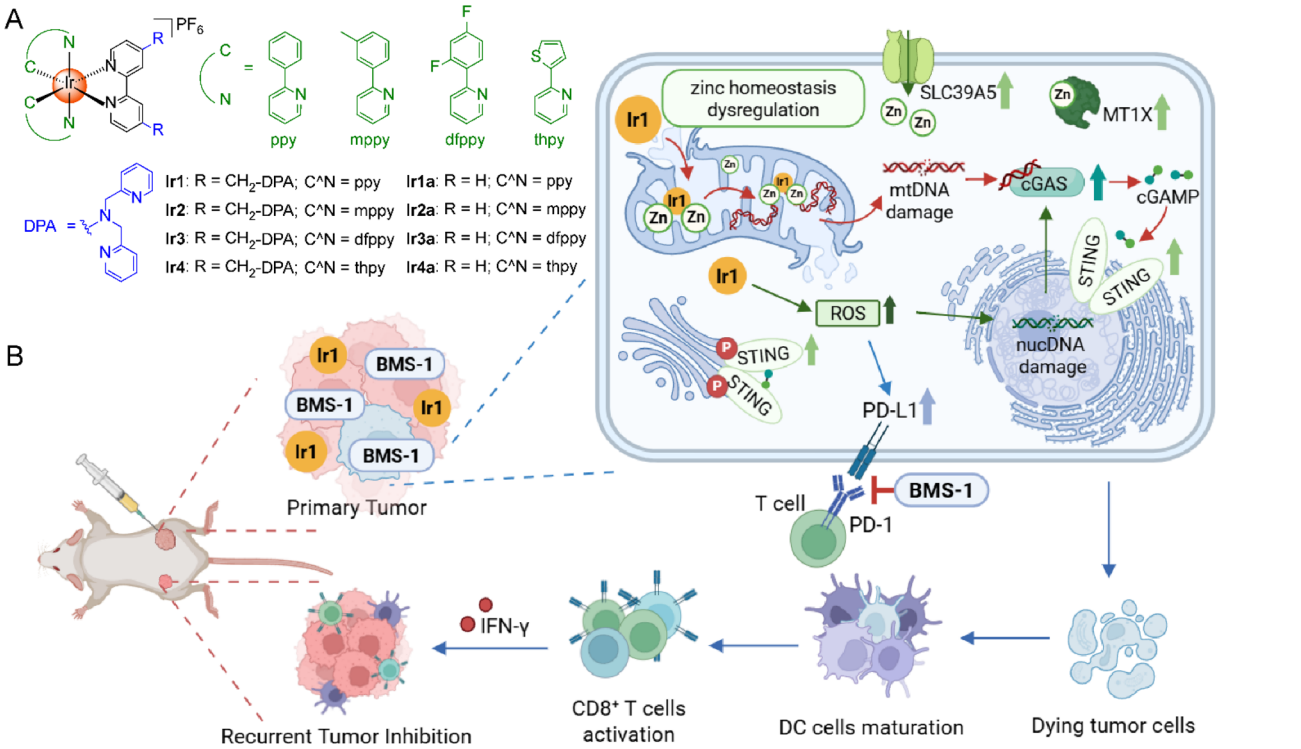

Scheme 1 (A) Chemical structures of **Ir1–Ir4** and **Ir1a–Ir4a**. (B) **Ir1** can actualize antitumor immunotherapy by dysregulating zinc homeostasis, inducing mtDNA cleavage and activating the cGAS-STING pathway. cGAMP: cyclic 5′-guanosine monophosphate (cGMP)-adenosine monophosphate (AMP); cGAS: cyclic GMP-AMP synthase; mtDNA: mitochondrial DNA; nucDNA: nuclear DNA; PD-1: programmed death-1; PD-L1: programmed death-ligand 1; ROS: reactive oxygen species; STING: stimulator of interferon genes. Created with BioRender.com (https://www.biorender.com/).

associated with cancer development and progression, with abnormal accumulation of zinc observed in breast cancer patients.[50,51] Researchers such as Lippard,[52] Guo,[46] Nam,[53–55] and Nagano[56] *et al.* designed numerous imaging probes for detecting changes in and localization of intracellular chelatable zinc.

Cyclometallic iridium complexes have gained widespread use in bioimaging and antitumor therapy attributed to their excellent photophysical and biochemical properties including large Stokes shifts, high photostability, two-photon absorption and long-lifetime phosphorescence emission, adjustable spectral characteristics, efficient cellular uptake with specific subcellular localization, diverse anti-tumor mechanisms and multi-target therapeutic mechanisms.[57–59] Ir(III) complexes have been reported as phosphorescent imaging agents for intracellular labile zinc.[53,60,61] These phosphorescent metal complexes exhibit strong binding capacity and effective imaging affinity for intracellular labile zinc, while their potential impacts on zinc homeostasis modulation and antitumor mechanisms have yet to be explored.

Based on the above studies, a series of cyclometallic Ir(III) complexes **Ir1–Ir4** with ditopic zinc ion-binding moiety 2,2′-dipicolylamine (DPA), are designed as mitochondrial DNA (mtDNA) nucleases activated by endogenous zinc (Scheme 1A). **Ir1–Ir4** can bind with 2 equiv. of Zn^{2+} *via* DPA moieties and exhibit a corresponding phosphorescence response. The most active complex, **Ir1**, can bind chelatable zinc in mitochondria and enrich intracellular zinc into mitochondria, which breaks the zinc homeostasis by affecting zinc regulatory proteins. Upon binding with Zn^{2+}, the as formed **Ir1-Zn$_2$** can bind to DNA more tightly, and act as mtDNA-targeted nucleases. By acting as a nuclease mimic to impair mtDNA and as a ROS producer to damage nuclear DNA (nucDNA), **Ir1** can further activate the cGAS-STING pathway. Finally, *in vivo* experiments demonstrate that the combination therapy of **Ir1** and programmed death-ligand 1 (PD-L1) inhibitor BMS-1 can effectively inhibit the growth of primary and recurrent tumors, highlighting its promising potential for antitumor immunotherapy. In summary, our work reports a phosphorescent Ir(III) complex that disrupts intracellular zinc homeostasis as well as utilizes endogenous metals to achieve artificial metalloenzyme simulation, providing a novel strategy for the activation of the cGAS-STING pathway.

Results and discussion

Ir1–Ir4 exhibit Zn^{2+}-responsive phosphorescence

Ir1 was synthesized by the literature method with slight modifications,[62] and **Ir2–Ir4** were synthesized using a similar method (Scheme S1). Briefly, the corresponding chloro-bridged precursors and the N^N ligand 4,4′-bis(dipicolylaminomethyl)-2,2′-bipyridine (dDPA-bpy) were heated to reflux in CH_2Cl_2/CH_3OH (2 : 1, v/v) for 6 h to obtain the crude product, which was further purified by silica gel column chromatography. **Ir1a–Ir4a** without the DPA moieties were synthesized as the controls, among

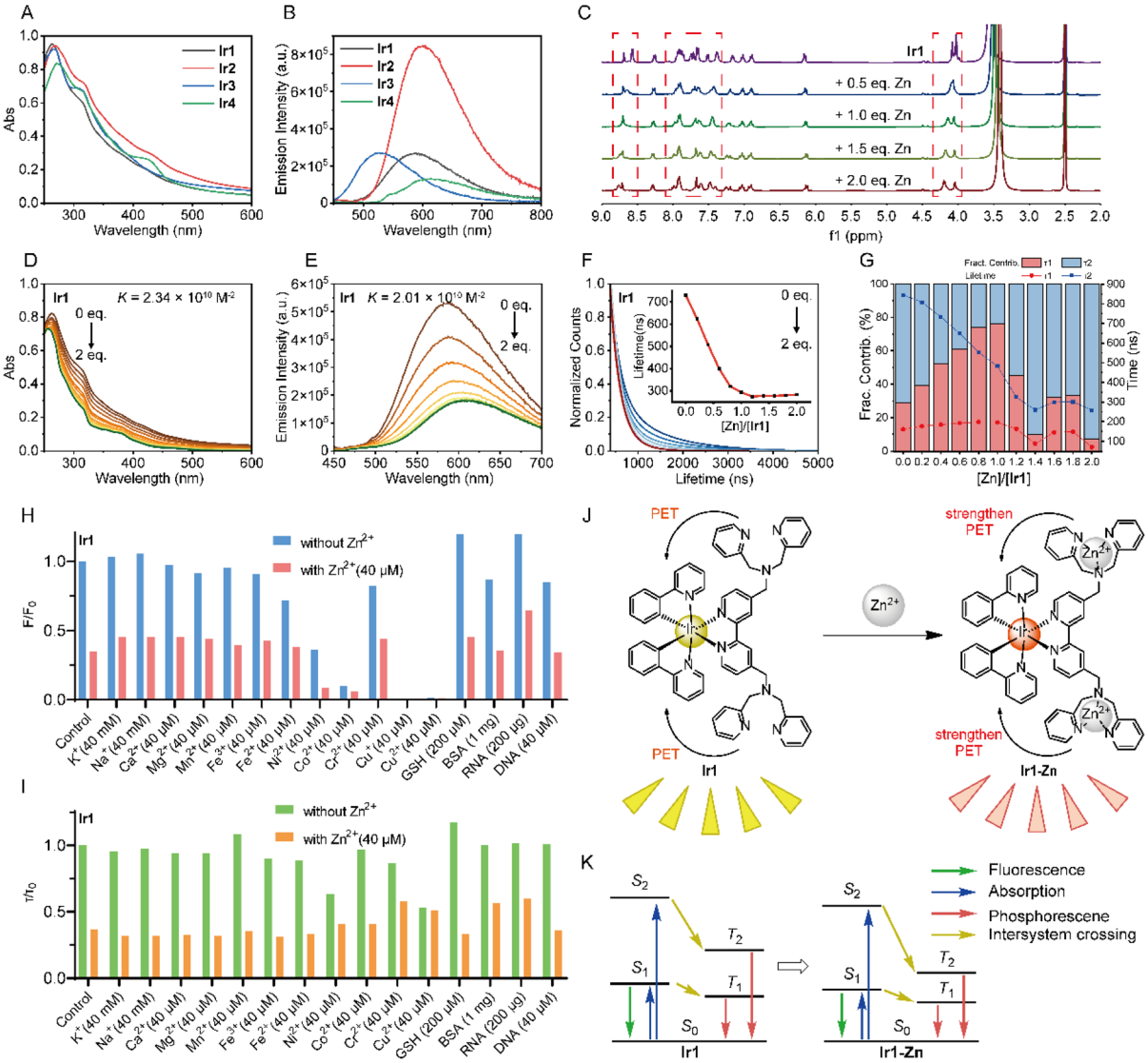

Fig. 1 **Ir1–Ir4** exhibit Zn^{2+}-responsive phosphorescence. (A) UV-Vis absorption spectra of **Ir1–Ir4** (20.0 μM) in PBS. (B) The emission spectra of **Ir1–Ir4** (20.0 μM) in degassed PBS. λ_{ex} = 405 nm. (C) ^{1}H NMR spectra of **Ir1** titrated with 0–2.0 equiv. Zn^{2+} in d^6-DMSO/H_2O. (D) The UV/Vis titration plots of **Ir1** (20.0 μM) with Zn^{2+} (0–2.0 equiv.) in the degassed PBS. (E) The phosphorescence titration plots of **Ir1** (20.0 μM) with Zn^{2+} (0–2.0 equiv.) in the degassed PBS. λ_{ex} = 405 nm. (F) Phosphorescence decay traces of **Ir1** (20 μM) upon titration with Zn^{2+} (0–2.0 equiv.) in degassed PBS. Inset: plots of phosphorescence lifetimes vary with the ratios of **Ir1** to Zn^{2+}. λ_{ex} = 405 nm. (G) The corresponding numerical lifetime and fractional contribution values of **Ir1** (20 μM) upon titration with Zn^{2+} (0–2.0 equiv.) in degassed PBS. (H) Histogram of phosphorescence intensity ratios of **Ir1** (20 μM) in 2 mL PBS at different states. (I) Histogram of phosphorescence lifetime ratios of **Ir1** (20 μM) in 2 mL PBS at different states. (J) The proposed PET mechanism of the phosphorescence response of **Ir1** towards Zn^{2+}. (K) Proposed energy level diagram for **Ir1** and **Ir1-Zn$_2$**.

which **Ir1a**, **Ir3a** and **Ir4a** were synthesized by the literature methods,[63–65] and **Ir2a** was synthesized by a similar method (Scheme S1). All the complexes were characterized by ESI-MS, ^{1}H NMR and ^{13}C NMR, and their purities were proved by HPLC (Fig. S1–S25).

The UV/Vis absorption spectra of **Ir1–Ir4** in PBS, CH_2Cl_2 and CH_3CN show the strong intra-ligand charge transfer (ILCT) at 250–320 nm and less intense spin-allowed/spin-forbidden metal-to-ligand charge transfer (^{1}MLCT/^{3}MLCT) at 320–500 nm (Fig. 1A, S26 and Table S1).[66] The absorption values of **Ir1–Ir4** at ILCT bands are higher than those of **Ir1a–Ir4a** (Fig. S26), which is caused by the increased energy of ILCT by DPA substitution. Under excitation at 405 nm, all the complexes emitted yellow-to-red emission in PBS, CH_2Cl_2 and CH_3CN, with quantum yields ranging from 0.002 to 0.16 and phosphorescence lifetimes ranging from 36.46 to 1485.53 ns (Fig. 1B, S27 and Table S1). The oil-water partition coefficients ($\log P_{o/w}$) of **Ir1–Ir4** range between 1.24 and 3.15, while $\log P_{o/w}$ of **Ir1a–Ir4a** range between −0.76 and −0.02 (Table S2), which indicates that **Ir1–Ir4** possess superior lipophilicity and biocompatibility to **Ir1a–Ir4a**. The UV/Vis absorption spectra exhibit a linear relationship between the absorbance and concentration of **Ir1**, **Ir3**, **Ir4** and **Ir1a–Ir4a** up to 100 μM in PBS buffer (with 1% DMSO, Fig. S28), demonstrating their sufficient aqueous solubility in aqueous media under the experimental conditions. The aqueous solubility of **Ir2** is within

40 μM, which can be attributed to its superior lipophilic character limiting its water solubility.

Job's plots of emission spectra confirm that **Ir1–Ir4** have 1 : 2 binding stoichiometry with Zn^{2+} (Fig. S29). Moreover, ^{1}H NMR spectra showed that H atoms of two DPA moieties display a low-field shift and the signal gradually weakens upon titration with Zn^{2+}, suggesting that **Ir1–Ir4** bind with Zn^{2+} through six N atoms of ditopic DPA moieties (Fig. 1C and S30). A hypochromic effect is observed for UV/Vis titration of **Ir1–Ir4** with Zn^{2+}, and the binding constants of **Ir1**, **Ir2**, **Ir3** and **Ir4** calculated by using the Benesi–Hildebrand equation are 2.34×10^{10}, 9.89×10^{9}, 8.26×10^{9} and 1.21×10^{10} M^{-2}, respectively (Fig. 1D, S31, S32 and Table S3).[67] Red shifts are observed upon the phosphorescence titration of **Ir1–Ir4** with Zn^{2+}, and the emission intensity of **Ir3** increases, whereas the other complexes show phosphorescence quenching. The binding constants of **Ir1**, **Ir2**, **Ir3** and **Ir4** obtained by emission titration are 2.01×10^{10}, 1.08×10^{10}, 1.02×10^{10} and 3.81×10^{10} M^{-2}, respectively (Fig. 1E, S31 and S32). These binding constants demonstrate that they have high Zn^{2+} binding affinity compared with the Zn^{2+} sensors reported previously.[68–70] Upon titration with Zn^{2+}, the phosphorescence decay curves show that Zn^{2+} can decrease the lifetimes of **Ir1–Ir4** (Fig. 1E, S33 and Tables S3–S6). For **Ir1**, the short lifetime component (τ_1) varies slightly in the range of about 70.74–198.04 ns. The long lifetime component (τ_2) quenches as the ratio of Zn^{2+}/**Ir1** increases, which can be utilized for intracellular two-photon phosphorescence lifetime imaging microscopy (TPPLIM) to analyze the cellular labile Zn^{2+} level (Fig. 1F). The control complexes **Ir1a–Ir4a** showed no response towards Zn^{2+}, further verifying that Zn^{2+} binds with **Ir1–Ir4** through DPA moieties (Fig. S34).

We screened the selectivity of the phosphorescence response of the complexes for various essential metal ions (K^+, Na^+, Ca^{2+}, Mg^{2+}, Mn^{2+}, Fe^{3+}, Fe^{2+}, Ni^{2+}, Co^{2+}, Cr^{3+}, Cu^+ and Cu^{2+}) and common biomolecules (GSH, BSA, RNA and DNA; Fig. 1H and S35A–C). Fe^{2+}, Fe^{3+} and Mn^{2+} can diminish the emission intensity of **Ir1–Ir4** to various degrees, and the biomolecules also have certain effects on them. After adding 2.0 equiv. of Zn^{2+}, **Ir1–Ir4** can reverse the phosphorescence changes and retain their response to Zn^{2+}, demonstrating their preferential binding selectivity for Zn^{2+}. Paramagnetic Ni^{2+}, Co^{2+} and Cu^{2+} can partially quench the emission of **Ir1–Ir4** and affect their responses to Zn^{2+}, and Cu^+ will completely quench the emission of **Ir1–Ir4**, which is similar to the Zn^{2+} sensors previously reported.[53,55,60,61] Most metal ions and biomolecules cannot affect the phosphorescence lifetime response of **Ir1–Ir4** to Zn^{2+}, except for paramagnetic Ni^{2+}, Co^{2+} and Cu^{2+} inhibiting the lifetime quenching effect of Zn^{2+} towards **Ir1–Ir4** to a certain degree (Fig. 1I and S33D–F). However, the significant disparity between the cellular concentrations of free copper ($\approx 10^{-3}$ fM)[71,72] and cellular labile zinc ($\approx$0.1–10^4 pM)[46] implies that Cu^{2+} and Cu^+ will show little effect on the phosphorescence responses of **Ir1** to intracellular Zn^{2+}.

The photophysical–chemical process of **Ir1–Ir4** titrated with Zn^{2+} can be explained by the photoinduced electron transfer (PET) mechanism.[73] Generally, Zn^{2+} will inhibit the PET process and enhance the emission intensity of "turn-on" sensors, such as **Ir3**.[55,60,61] For **Ir1**, **Ir2** and **Ir4**, the coordination of DPA moieties with Zn^{2+} will strengthen their PET process and quench the phosphorescence emission (Fig. 1J).[53,73,74] However, considering that there are two coordination centers in one complex molecule, the intramolecular interactions among different ligands and metal centers are too intricate to partition the complexes into phosphorescence structures and ionophore structures.[75] Thus, the PET mechanism can only crudely explain the phosphorescence response of the compounds towards Zn^{2+}.

Therefore, density functional theory (DFT) and time-dependent density functional theory (TD-DFT) were further applied to examine the energy change of **Ir1** titrated with Zn^{2+}. **Ir1** has a group of triplet excited states composed of complicated intramolecular electron transitions (Table S7). The first triplet state T_1 is constructed from the highest occupied molecular orbital (HOMO) to the lowest unoccupied molecular orbital (LUMO) transition, assignable as triplet metal-to-ligand charge transfer (^{3}MLCT) and triplet ligand-to-ligand charge transfer (^{3}LLCT, Fig. S36). The second triplet state T_2 arises from HOMO−8 (27.2%), HOMO−2 (20.7%), HOMO−4 (14.6%) to the LUMO, which can be attributed to ^{3}MLCT, $^3L_{C^N}L_{N^N}CT$ and triplet intra-ligand charge transfer ($^3IL_{N^N}CT$, Fig. S36).[60] DFT calculations of the adduct of **Ir1** with 2 equiv. of Zn^{2+} (**Ir1-Zn$_2$**) show that the HOMO energy level of **Ir1-Zn$_2$** is close to that of **Ir1**, while the LUMO energy level of **Ir1-Zn$_2$** is lower than that of **Ir1** (Fig. S37). The narrowed energy gap explains the red-shift emission of **Ir1** upon titration with Zn^{2+}.[74] In addition, HOMO−8, HOMO−2, and HOMO−4 orbitals of **Ir1-Zn$_2$** are stabilized, which is significantly different from those of complex **Ir1**, implying that the binding of Zn^{2+} causes a significant change in the intramolecular charge distribution of **Ir1** (Fig. S37). The composition of higher-energy $^3L_{C^N}L_{N^N}CT$ decreases, while the composition of lower-energy $^3IL_{N^N}CT$ increases, resulting in a decrease in the energy of T_2, shortening the phosphorescence lifetime and reducing the emission intensity of T_2 (Fig. 1K). Additionally, a significant reduction in the T_2 excited state energy to a similar energy of T_1 interferes with the photon release from T_1 to S_0. The increase of the energy gap between S_2 and T_2 is unfavorable for the intersystem crossing (ISC) of electrons and the accumulation of triplet excitons, which further leads to the weakening of the phosphorescence emission (Fig. 1K).

Ir1–Ir4 show potent antiproliferative activity *in vitro*

It has been reported that the zinc content in breast cancer cells is abnormally higher than that in normal breast tissue,[51] which encourages us to explore the antitumor activities of **Ir1–Ir4** on breast cancer cell lines. The antiproliferative activity of **Ir1–Ir4** on human triple negative breast cancer (MDA-MB-231), human breast cancer (MCF-7), mouse triple negative breast cancer (4T1), human normal breast epithelial cells (MCF-10A) and cervical cancer cells (HeLa) was assessed by MTT assay (Table 1). The growth inhibitory activities of **Ir1–Ir4** in MDA-MB-231 cells are about 12.3–51.7 times that of cisplatin. The order of growth inhibitory activities of **Ir1–Ir4** towards MDA-MB-231 cells is as follows: **Ir2** ≈ **Ir4** > **Ir1** > **Ir3**. However, the IC_{50} of complexes in

Table 1 Cytotoxicity (IC_{50}, μM) of the tested compounds on different cell lines[a]

Complex	MDA-MB-231	MCF-7	4T1	MCF-10A	HeLa
Ir1	0.85 ± 0.05	3.72 ± 0.16	8.70 ± 0.49	2.85 ± 0.28	1.88 ± 0.35
Ir2	0.39 ± 0.02	1.60 ± 0.05	3.02 ± 0.48	1.29 ± 0.09	1.12 ± 0.02
Ir3	1.64 ± 0.10	2.30 ± 0.16	4.83 ± 0.90	2.41 ± 0.25	1.17 ± 0.05
Ir4	0.42 ± 0.04	3.53 ± 0.71	4.60 ± 0.74	2.88 ± 0.11	1.27 ± 0.44
Cisplatin	20.16 ± 5.60	18.30 ± 5.74	25.50 ± 2.52	15.50 ± 4.33	8.35 ± 0.86

[a] Cells were incubated with the compounds for 72 h. Data are presented as the means ± standard deviations (SD).

MCF-10A cells is ordered as follows: **Ir2** > **Ir3** > **Ir1** ≈ **Ir4**. The IC_{50} of **Ir1a–Ir4a** on MDA-MB-231 cells falls within the range of 3.3–6.3 μM, in which **Ir1a** is 7.4-fold less active than **Ir1** (Table S8). Additionally, studies indicate that cervical cancer cells exhibit low zinc levels,[76] which is validated by inductively coupled plasma-mass spectrometry (ICP-MS, Fig. S38). MTT assays demonstrate that **Ir1–Ir4** and **Ir1a–Ir4a** exhibit comparable toxicity in HeLa cells (Table 1 and S8), suggesting that the zinc-targeting design of **Ir1–Ir4** enhances their cytotoxic effects in breast cancer cells with elevated zinc content. These results prove that **Ir1–Ir4** possess strong anti-proliferative activities against breast cancer cell lines.

Ir1 colocalizes with Mito-Tracker Deep Red (MTDR) with a high Pearson's correlation coefficient (PCC = 0.93–0.96, Fig. 2A), while it localizes weakly with ER-Tracker Red (ETR, PCC = 0.78) or Lyso-Tracker Red (LTR, PCC = 0.52, Fig. S39). Significantly, **Ir1** is already localized to mitochondria after 15-minute incubation in MDA-MB-231 cells, and MTDR exhibits mitochondrial filamentous structures. Mitochondrial damage occurs in MDA-MB-231 cells treated with **Ir1** for 30 minutes, revealing some punctate structures. At 1 hour, MTDR displays a greater number of punctate structures, confirming that **Ir1** caused severe mitochondrial damage. Meanwhile, colocalization experiments show that **Ir2–Ir4** and **Ir1a–Ir4a** are mainly localized in mitochondria after 1-h incubation (Fig. S40).

The cellular uptake capabilities of **Ir1–Ir4** in MDA-MB-231 cells were measured by ICP-MS (Fig. 2B). Although all the complexes are accumulated in the mitochondria of MDA-MB-231 cells, **Ir1** shows the highest cellular uptake levels. The total cellular uptake of **Ir1** is 1.5–3.0 times that of **Ir2–Ir4**, while its mitochondrial uptake is 1.3–2.8 times that of **Ir2–Ir4**. We further investigated the cellular uptake levels of **Ir1a–Ir4a**, which were lower than those of **Ir1–Ir4** (Fig. S41). Considering the antitumor activities and mitochondrial accumulation levels of **Ir1–Ir4**, **Ir1** was selected for further study.

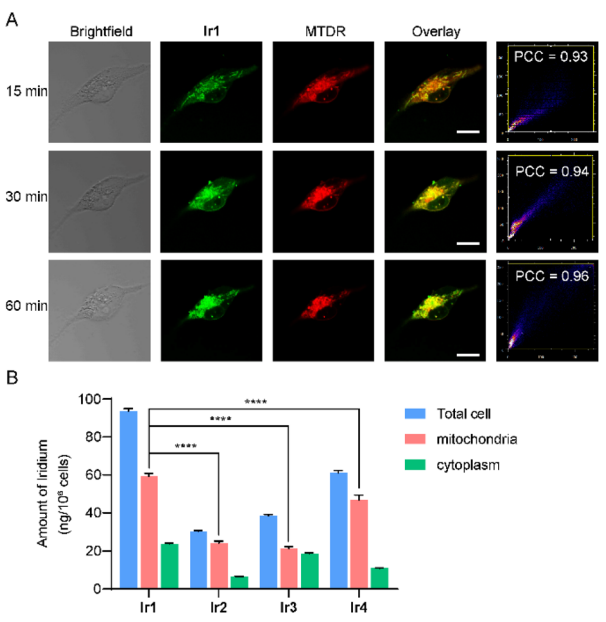

Fig. 2 **Ir1** can accumulate in mitochondria. (A) Colocalization images of **Ir1** with MTDR in MDA-MB-231 cells. Cells were treated with **Ir1** (2 μM) and incubated with MTDR (100 nM, 15 min). **Ir1**: λ_{ex} = 405 nm; λ_{em} = 600 ± 20 nm. MTDR: λ_{ex} = 633 nm. λ_{em} = 660 ± 10 nm. Scale bar: 10.0 μm. (B) Cellular iridium content measured by ICP-MS. MDA-MB-231 cells were treated with **Ir1–Ir4** (2 μM) for 1 h.

Ir1 can image chelatable Zn^{2+} by TPPLIM and affect intracellular zinc homeostasis

As the long-lifetime component (τ_2) value of **Ir1** shows a good linear response to the change of the proportion of bound Zn^{2+}, we chose **Ir1** for further studies. Two-photon phosphorescence lifetime imaging microscopy (TPPLIM) shows that the fitted value of τ_2 is approximately 900 ns at 15 min, which corresponds to the τ_2 lifetime of **Ir1** alone. After 1 h, τ_2 of **Ir1** decreases to approximately 600 ns, and the TPPLM image at 6 h is similar to that at 1 h (Fig. 3A). By correspondence analysis with the previous phosphorescence lifetime measurements (Fig. 3B), these results show that the concentration ratio of Zn^{2+} to **Ir1** was about 0.6 (Fig. 3C), indicating that about 30% of **Ir1** binds to labile Zn^{2+} in mitochondria at this point. ICP-MS measurement shows that both cellular zinc content and mitochondrial zinc content are increased in **Ir1**-treated cells, confirming that **Ir1** induces the accumulation of zinc in mitochondria (Fig. 3D). Furthermore, the treatment with **Ir1** elevated zinc levels in the nucleus, but did not significantly alter ER zinc content (Fig. S42). This compartment-specific effect indicates dysregulation of cellular zinc homeostasis. In contrast, although **Ir1a** also tends to accumulate in mitochondria, it shows minimal impact on zinc contents in whole cells and mitochondria (Fig. 3D).

To further confirm the effects of **Ir1** on Zn^{2+} cellular homeostasis, we analyzed the proteins related to zinc homeostasis regulation from RNA-sequencing (RNA-seq) data. A series

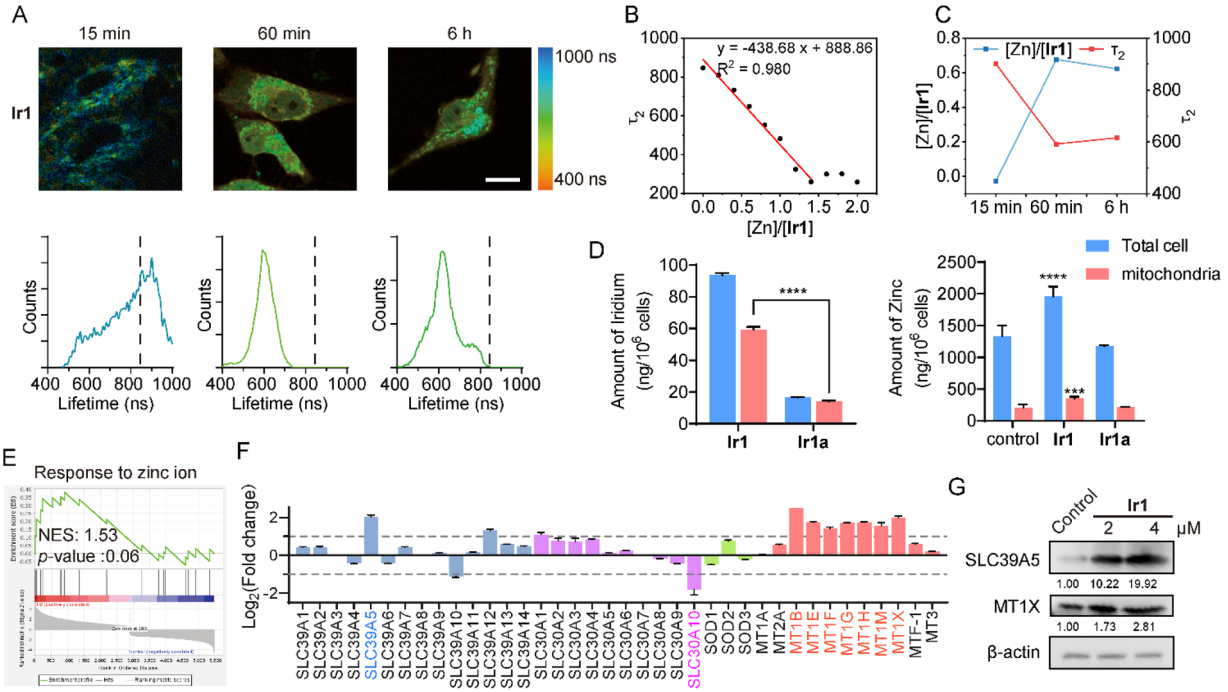

Fig. 3 **Ir1** can image chelatable Zn^{2+} by TPPLIM and dysregulate intracellular zinc homeostasis. (A) TPPLIM measurement of the changes in the long-lifetime component (τ_2) of **Ir1** (2 μM) in MDA-MB-231 cells. λ_{ex} = 810 nm (two-photon); λ_{em} = 550 ± 20 nm. Scale bar: 10.0 μm. (B) The fitted plot of the τ_2 value varies with the ratio of Zn^{2+} to **Ir1** upon titration with Zn^{2+} in degassed PBS. (C) Trend chart showing the calculated τ_2 value and the ratio of Zn^{2+} to **Ir1** in the MDB-MA-231 cells incubated with **Ir1**. (D) Cellular iridium and zinc contents measured by ICP-MS. MDB-MA-231 cells were treated with **Ir1**/**Ir1a** (2 μM) for 1 h. The data are presented as the means ± SD of three independent experiments. ***$p < 0.001$ and ****$p < 0.0001$, compared with the control group. (E) GSEA reveals the negative and positive enrichment of genes altered in the process responding to Zn^{2+}. NES: normalized enrichment score. (F) RT-qPCR analysis of Zn^{2+} regulatory protein related genes in **Ir1**-treated MDA-MB-231 cells. (G) Western blot analysis showing the impact of **Ir1** on the expression of the indicated proteins. Cells were treated with **Ir1** at the indicated concentrations for 24 h.

of Zn^{2+}-regulated proteins is dysregulated in **Ir1**-treated cells, confirming the dysregulation of zinc homeostasis due to intervention in the expression of zinc-related proteins within cells (Table S11). Gene set enrichment analysis (GSEA) shows that the response to zinc ions is upregulated in the **Ir1**-treated group (Fig. 3E). The alterations in the expression of zinc-related proteins caused by **Ir1** treatment are also detected by the real-time quantitative polymerase chain reaction (RT-qPCR, Fig. 3F). After treatment with **Ir1**, the ZIP family protein SLC39A5 is up-regulated by 2.04-fold, whereas the expression of ZnT family protein SLC30A10 is significantly down-regulated by about 1.80-fold. Most of the MT proteins for Zn^{2+} buffering and storage are also up-regulated to various degrees. Western blot detects that the expression levels of SLC39A5 and MT protein MT1X are up-regulated, conforming with the results of the RT-qPCR (Fig. 3G). Given that MT1X is mainly expressed in the cell nucleus,[77] its upregulation can explain the increase in zinc content in the cell nucleus induced by **Ir1**. From these data, we propose that **Ir1**-treatment increases the intracellular level of Zn^{2+} by dysregulating zinc transporter proteins and metallothioneins, and further sequesters mitochondrial labile zinc by targeting mitochondria.

Ir1 acts as a mtDNA-targeted nuclease mimic upon Zn^{2+} binding

Due to the fact that zinc is the active center of nucleases, and it has been reported that simple zinc complexes can mimic the activity of nucleases,[78] we then studied the DNA binding and cleavage activities of **Ir1** and its Zn^{2+}-binding form **Ir1-Zn$_2$**. The binding constants of **Ir1** and **Ir1-Zn$_2$** towards calf thymus DNA (ct-DNA) measured by UV/Vis titration are (2.18 ± 0.17) × 10^5 M^{-1} and (3.11 ± 0.37) × 10^5 M^{-1}, respectively, which indicates that they possess moderate DNA binding affinities (Fig. 4A and B). The binding constants of **Ir1** and **Ir1-Zn$_2$** obtained by emission titration are (1.24 ± 0.46) × 10^5 M^{-1} and (3.15 ± 1.23) × 10^5 M^{-1}, respectively (Fig. 4C and D), which also indicates that binding of Zn^{2+} can increase the DNA binding affinity of **Ir1**. Upon DNA binding, the emission intensity of **Ir1** and **Ir1-Zn$_2$** is decreased and increased, respectively, which implies their different DNA binding modes. Agarose gel electrophoresis shows that **Ir1** or Zn^{2+} alone can't cleave plasmid DNA, while **Ir1-Zn$_2$** can cause DNA degradation (Fig. 4E), indicating the nuclease mimetic activity of **Ir1-Zn$_2$**.

Molecular docking studies show that the binding energies of **Ir1** and **Ir1-Zn$_2$** with double-stranded DNA (ds-DNA) are (−8.32 ± 0.49) and (−9.77 ± 0.68) kcal mol^{-1}, respectively, which further proves that Zn^{2+} coordination increases the DNA-binding capabilities of **Ir1** (Tables S9 and S10). The most

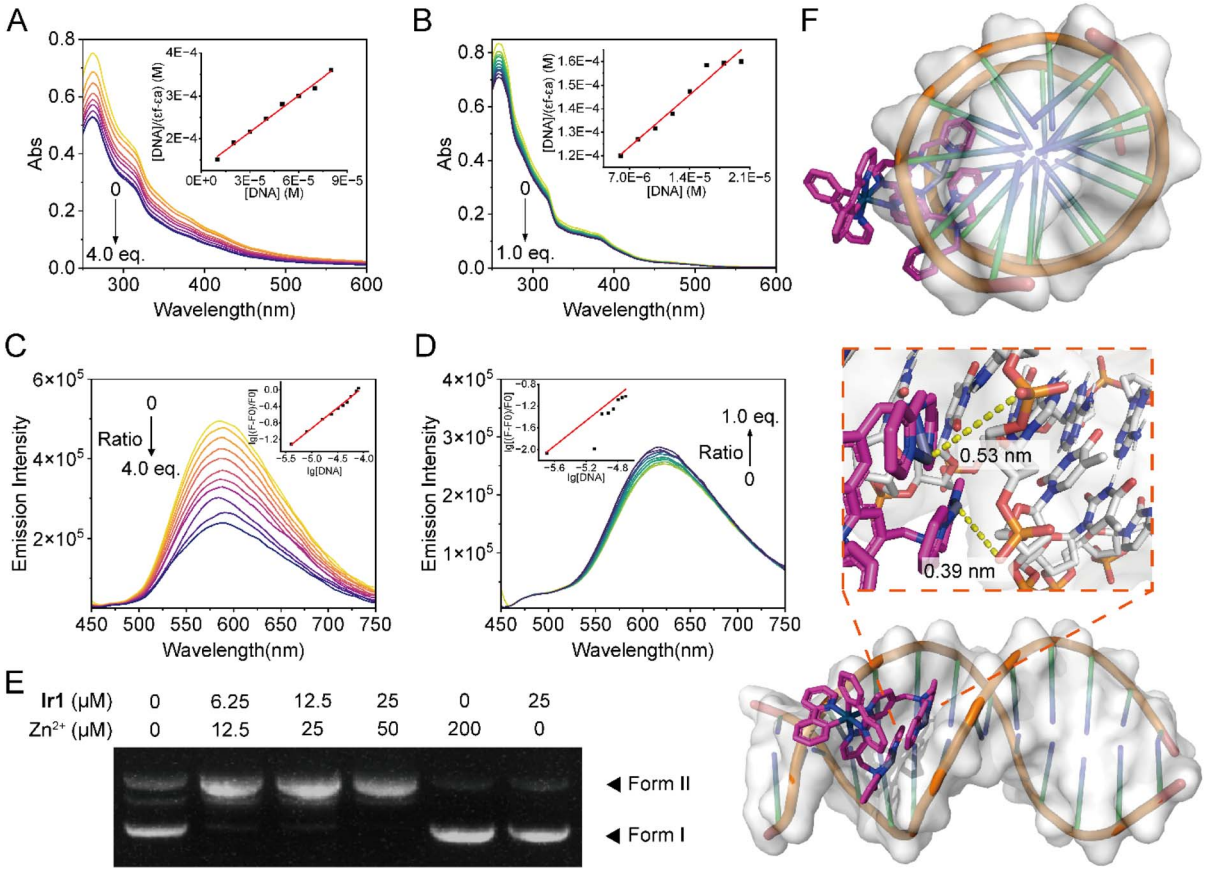

Fig. 4 The DNA binding and cleavage activity of **Ir1** and **Ir1-Zn$_2$**. (A and B) UV/Vis titration of **Ir1** (20 μM, A) and **Ir1-Zn$_2$** (20 μM, B) with ct-DNA in Tris–HCl buffer (pH 7.4, 100 mM NaCl). (C and D) Emission titration of **Ir1** (20 μM, C) and **Ir1-Zn$_2$** (20 μM, D) with ct-DNA in Tris–HCl buffer. (E) Agarose gel electrophoresis of the pBR322 plasmid (400 ng) treated with different concentrations of **Ir1** and $ZnCl_2$ for 8 h at 37 °C in Tris–HCl buffer (pH 7.4, 100 mM NaCl). Form I/II: supercoiled/nicked DNA. (F) Molecular docking studies of **Ir1-Zn$_2$** with ds-DNA (PDB: 5t4w). Inset: the distances between Zn ions and O atoms.

stabilized configuration from docking shows that **Ir1** and **Ir1-Zn$_2$** are located within the minor groove (Fig. 4F and S41). The viscosity of ct-DNA decreases slightly in the presence of **Ir1** or **Ir1-Zn$_2$**, which verifies that compounds are more likely to bind within the DNA grooves, causing the DNA helix to bend and twist, thereby reducing its effective length and consequently lowering the viscosity (Fig. S42).[79] Hydrophobic interactions between ds-DNA and **Ir1-Zn$_2$** stabilized the docking form, prompting the DPA moieties of **Ir1-Zn$_2$** to intercalate into ds-DNA more thoroughly than **Ir1**. Generally, zinc complexes cleave DNA through hydrolysis of phosphodiester bonds and nucleophilic attack.[80] The molecular docking calculation shows that the distances between Zn ions and oxygen atoms of phosphodiester bonds are 0.39 and 0.53 nm (Fig. 4F), which implies the existence of the weak interactions and the potential trend for DNA hydrolysis.

Ir1 activates the cGAS-STING pathway by damaging mtDNA

Transmission electron microscopy (TEM) observation reveals that **Ir1** triggers necrosis, with notable mitochondrial damage and numerous cytoplasmic vacuoles (Fig. 5A). The type of cell death of **Ir1** was investigated by measuring the cell viabilities of MDA-MB-231 cells with pretreatment of different cell death inhibitors for 1 h and further treatment of **Ir1** (10 μM, 24 h). Only the necrostatin-1 (Nec-1, necroptosis inhibitor) and necrosulfonamide (NSA, necroptosis inhibitor) can improve the cell viabilities of MDA-MB-231 cells with treatment of **Ir1**, suggesting that **Ir1** can induce necrosis (Fig. 5B). Otherwise, Z-VAD-FMK (pan-caspase inhibitor), 3-methyladenine (3-MA, autophagy inhibitor), ferrostatin-1 (Fer-1, ferroptosis inhibitor) and liproxstatin-1 (Lip-1, ferroptosis inhibitor) show limited effects on inhibition of antiproliferative activities of **Ir1**.

The reactive oxygen species (ROS) levels in MDA-MB-231 cells increase in a dose-dependent manner after **Ir1** treatment (Fig. 5C). As measured by 2′,7′-dichlorodihydrofluorescein diacetate (DCFH-DA) staining and flow cytometry, the cellular ROS values increase 7-fold in MDA-MB-231 cells incubated with **Ir1** at a concentration of 16 μM for 6 h. In addition, 96% of MDA-MB-231 cells show depolarized mitochondria with lost mitochondrial membrane potential (MMP) after 4-μM **Ir1** treatment for 6 h, as measured by 5,5′,6,6′-tetrachloro-1,1′,3,3′-tetraethylbenzimidazolyl-carbocyanine iodide (JC-1) staining and flow cytometry (Fig. 5D). The human mitochondrial genome encodes 37 genes, including 13 critical genes that

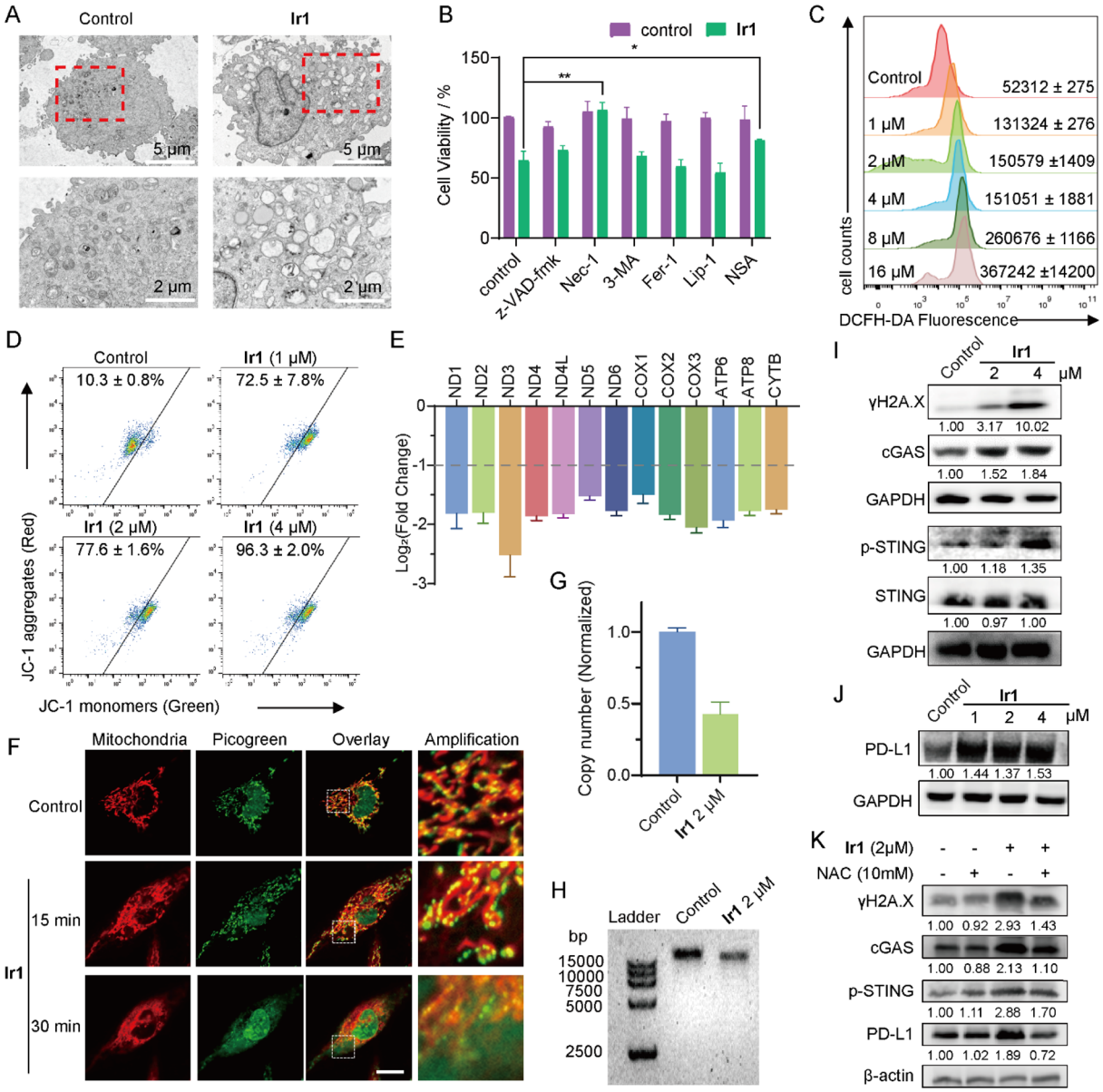

Fig. 5 (A) TEM images of MDA-MB-231 cells treated with **Ir1** (2 μM, 6 h). (B) The impact of different cell death inhibitors on the antiproliferative activities of **Ir1** (10 μM, 24 h). The data are presented as the means ± SD of three independent experiments. *$p < 0.05$ and **$p < 0.01$, compared with the control group. (C) Flow cytometry measurement of cellular ROS in MDA-MB-231 cells treated with **Ir1** at the indicated concentrations for 6 h. (D) Impact of **Ir1** on MMP measured by JC-1 staining and flow cytometry. $\lambda_{ex} = 488$ nm; $\lambda_{em} = 530 \pm 30$ nm (Green)/590 ± 30 nm (Red). MDA-MB-231 cells were treated with **Ir1** at the indicated concentrations for 6 h. (E) The expression of 13 genes encoded by the mitochondrial genome in **Ir1**-treated (2 μM, 24 h) MDA-MB-231 cells. (F) Colocalization of MTDR with PicoGreen in MDA-MB-231 cells. Cells were treated with **Ir1** (2 μM) and incubated with PicoGreen (1 μg mL^{-1}, 15 min) and MTDR (100 nM, 15 min). **Ir1**: $\lambda_{ex} = 405$ nm; $\lambda_{em} = 600 \pm 20$ nm. PicoGreen: $\lambda_{ex} = 488$ nm, $\lambda_{em} = 520 \pm 20$ nm. MTDR: $\lambda_{ex} = 633$ nm. $\lambda_{em} = 660 \pm 10$ nm. Scale bar: 10 μm. (G) Impact of **Ir1** on the mtDNA copy number. (H) Gel electrophoresis of mtDNA breakage in **Ir1**-treated MDA-MB-231 cells. (I–K) Western blot analysis showing the impact of **Ir1** on the expression of the indicated proteins. Cells were treated with **Ir1** at the indicated concentrations for 24 h.

encode essential components of the oxidative phosphorylation (OXPHOS) system.[81] RNA-seq reveals that the expression of the 13 genes encoded by the mitochondrial genome is attenuated (|fold change| ≥ 2; false discovery rate ≤ 0.05, Table S12). The real-time quantitative polymerase chain reaction (RT-qPCR) shows that the expression of all 13 genes in **Ir1**-treated MDA-MB-231 cells is down-regulated by 1.50–2.51 times (fold change >2, Fig. 5E), further demonstrating that **Ir1** can effectively damage mitochondrial function through generation of ROS and disruption of mitochondrial gene expression.

In addition, the morphology of mitochondria gradually disperses from a clear filamentous structure in **Ir1**-treated cells (Fig. 5F). After 15–30 min treatment, the fluorescence of PicoGreen gradually separates from that of MTDR, suggesting that mtDNA is released in the cytoplasm. In contrast, MTDR and PicoGreen show a good co-localization pattern in control cells.

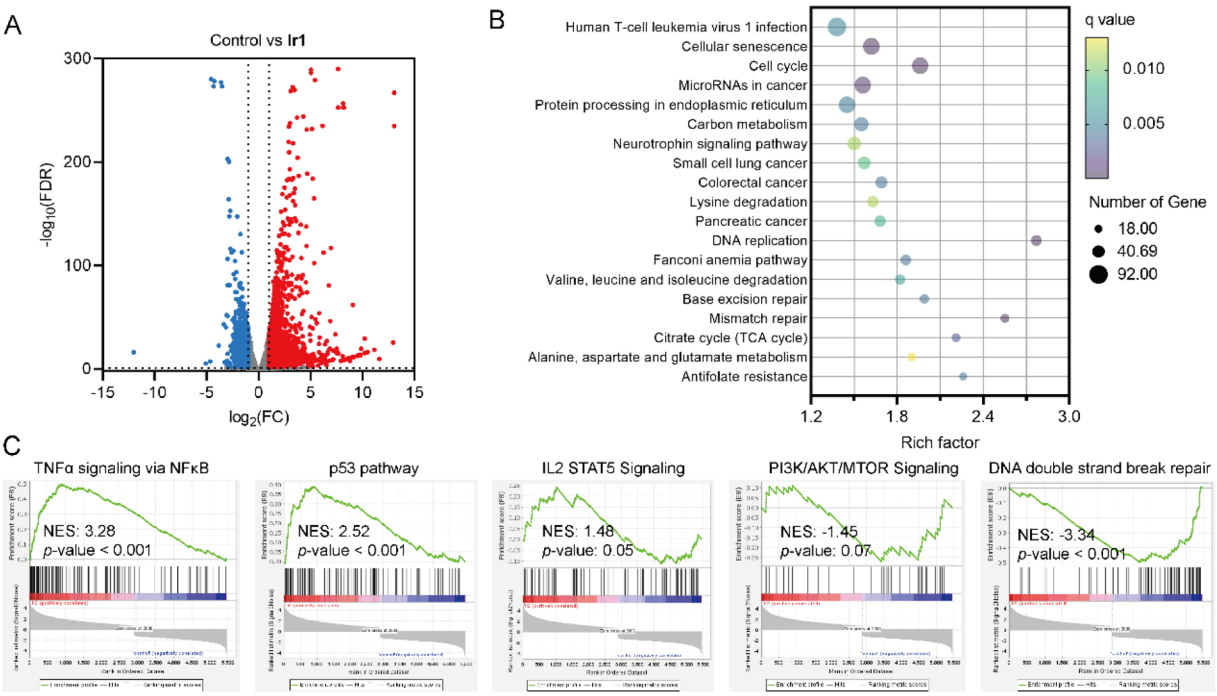

Fig. 6 Impact of **Ir1** on the transcriptome. (A) Volcano plots show the differentially expressed genes in **Ir1**-treated (2 μM, 6 h) MDA-MB-231 cells. (B) KEGG enrichment analysis of the DEGs in **Ir1**-treated MDA-MB-231 cells. (C) GSEA reveals the negative and positive enrichment of genes altered in various cellular processes. NES: normalized enrichment score.

Additionally, **Ir1a** can't induce the dispersion of fluorescence of MTDR and PicoGreen, indicating its disability to damage mtDNA (Fig. S43). After **Ir1** treatment (2.0 μM), the copy number of mtDNA is reduced by about 58% compared with that of nuclear DNA (nucDNA; Fig. 5G). Gel electrophoresis reveals that **Ir1** causes significant mtDNA fragmentation in MDA-MB-231 cells (Fig. 5H). Meanwhile, the expression of γH2A.X, a marker of nuclear DNA damage and repair, is dose-dependently up-regulated after **Ir1** treatment (Fig. 5I). Incubation of *N*-acetylcysteine (NAC, an ROS scavenger) can partially reduce the expression of γH2A.X, which indicates that **Ir1** also induces nucDNA damage through generation of ROS (Fig. 5K). Western blot detects that the expression levels of cGAS and p-STING are elevated (Fig. 5I), while NAC treatment partially abrogates cGAS and p-STING expression (Fig. 5K), demonstrating that **Ir1** activates the cGAS-STING pathway through nucDNA damage as an ROS producer and mtDNA damage as nuclease mimics. It has been reported that PD-L1 expression is related to ROS accumulation.[82] Western blot confirms that **Ir1** can increase the expression of PD-L1 in MDA-MB-231 cells (Fig. 5J), and NAC can substantially reduce **Ir1**-induced PD-L1 upregulation (Fig. 5K), which inspires us to investigate whether **Ir1** can synergize with immune checkpoint inhibition *in vivo*.

Impact of Ir1 on the transcriptome

RNA-sequencing (RNA-seq) was performed to further investigate the impact of **Ir1** on the gene expression pattern. The correlation coefficients between every two individual samples from the same group are greater than 0.95 (Fig. S44), indicating that the data are repeatable. Cluster analysis and the heatmap show that the differentially expressed genes (DEGs) induced in the **Ir1**-treated cells present a significant difference in expression patterns compared to the control group, suggesting the reproducibility of the data (Fig. S45). 4756 significantly differentially expressed genes (|fold change| ≥ 2; false discovery rate ≤0.05; upregulated: 3149 genes; downregulated: 1607 genes) are detected in **Ir1**-treated cells compared with the control cells (Fig. 6A).

Gene Ontology (GO) enrichment analysis reveals that **Ir1** mainly influences the DNA replication, cell cycle, nucleus, mitochondrion, DNA binding, ATP binding and ion channel binding (Fig. S46–S48). Kyoto Encyclopedia of Genes and Genomes (KEGG) enrichment analysis shows that **Ir1** mainly influences DNA replication, cell cycle and mismatch repair (Fig. 6B). Gene set enrichment analysis (GSEA) shows that TNF-α signaling *via* the NF-κB, p53 pathway and IL2 STAT5 signaling are upregulated in the **Ir1**-treated group, while DNA double strand break repair and PI3K/AKT/mTOR signaling are dysregulated in the **Ir1**-treated group (Fig. 6C). These results suggest that **Ir1** mainly exerts its anticancer effects through the induction of DNA damage and immune responses.

Ir1 synergistically acts with ICIs to effectively improve the immune TMEs

Recent studies highlight that the depletion of PD-L1 is associated with STING activation, which can inhibit cancer growth.[83] The Cancer Genomic Atlas (TCGA) database analysis shows that the correlation *R*-values of PD-L1 with cGAS and STING reach 0.51 and 0.31 (*p*-values <0.001, Fig. 7A), respectively, indicating that they are closely associated. As one of the small-molecule

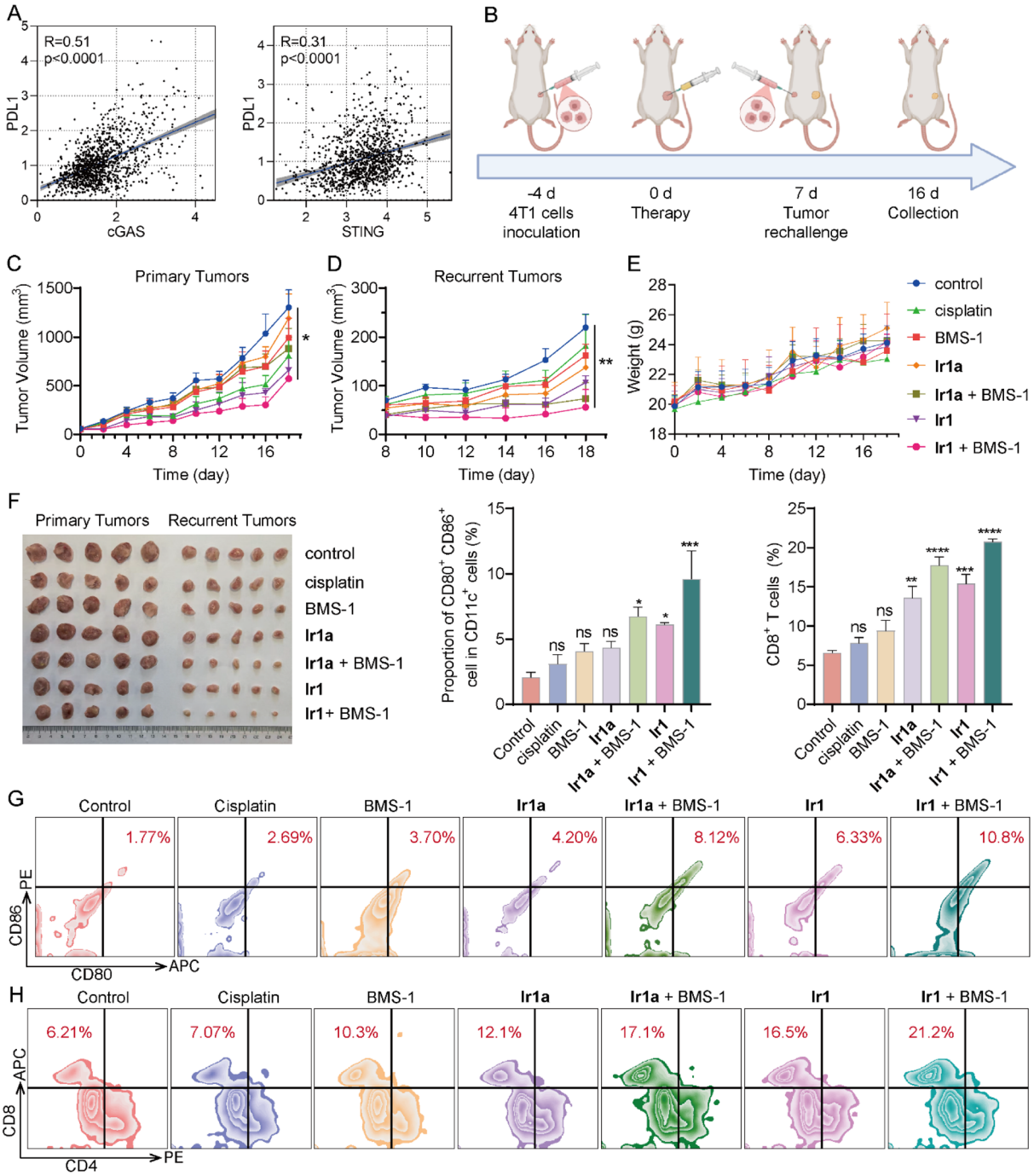

Fig. 7 **Ir1** synergistically acts with ICIs to effectively improve the immune TMEs. Mice were randomized into 7 groups (control, cisplatin, BMS-1, **Ir1**, **Ir1a**, **Ir1** + BMS-1, and **Ir1a** + BMS-1). (A) Correlation analysis of PD-L1 with cGAS and STING of BRCA using the TCGA database. (B) Schematic illustration of the *in vivo* therapeutic protocol. (C) Volume curves of the primary tumors. (D) Volume curves of the recurrent tumors. (E) Body weight curves of mice. (F) The photographs of the primary and recurrent tumors at the end of treatment. (G) Quantitative measurement of the proportions of CD80+ and CD86+ cells in recurrent tumors at the end of the treatment by flow cytometry ($n = 3$). (H) Quantitative measurement of the proportions of CD4+ and CD8+ cells in recurrent tumors at the end of the treatment by flow cytometry ($n = 3$). The data are presented as the means ± SD of three independent experiments. *$p < 0.05$, **$p < 0.01$, ***$p < 0.001$, and ****$p < 0.0001$, compared with the control group.

PD-L1 inhibitors, BMS-1 has been extensively utilized in various antitumor studies,[84–86] and it is chosen as the synergistic ICI drug with **Ir1**.

To assess the biodistribution of **Ir1**, we administered **Ir1** (5 mg kg^{-1}) *via* intratumoral injection to tumor-bearing mice and measured drug concentrations in tissues, tumors, and blood at 24 hours, 48 hours, and 7 days post-administration (Fig. S49). ICP-MS analysis revealed iridium accumulation within tumors at 24 h, decreasing by approximately 27.2% at 48 hours, with residual intertumoral levels of 2.9% at 7 days. Following

administration, the drug accumulated in the liver and kidneys, with both organs showing significant reduction by day 7. Concentrations in blood decreased by approximately 93.2% at day 7 compared to 24 h post-administration. These results confirm that the drug undergoes metabolism *via* the liver and kidneys and there is almost no drug residue in the mice after 7 days of administration. Blood routine tests further demonstrate that hematological parameters are all in the normal range, indicating that **Ir1** has no obvious toxicity in mice (Fig. S50).

We established a tumor rechallenge model to evaluate immunization vaccination, thereby evaluating the effectiveness of tumor immunotherapy (Fig. 7B). 4T1 cells (1×10^6 cells/100 μL PBS) were inoculated subcutaneously into BALB/C female mice as primary tumors. 4 days later, mice were randomized into 7 groups (control, cisplatin, BMS-1, **Ir1**, **Ir1a**, **Ir1** + BMS-1, and **Ir1a** + BMS-1), followed by a single intertumoral treatment with corresponding drugs (5 mg kg^{-1}). After 7 days, 4T1 cells (2×10^6 cells/100 μL PBS) were implanted contralaterally as recurrent tumors. Tumor volume and body weight were monitored for 18 days post-administration.

At the end of treatment, the suppression effects on primary tumors are ordered as follows: **Ir1** + BMS-1 > **Ir1** > cisplatin > BMS-1 ≈ **Ir1a** + BMS-1 > **Ir1a** (Fig. 7C and F), suggesting that **Ir1** alone or in combination with BMS-1 has an optimal antitumor effect compared to cisplatin and **Ir1a** alone or in combination with BMS-1. Simultaneously, the inhibition rates of **Ir1** + BMS-1 and **Ir1a** + BMS-1 on recurrent tumors are 74.5% and 66.4%, showing better performance compared with the inhibition rates of **Ir1**, **Ir1a** (37.2%), cisplatin (16.9%), and BMS-1 (25.9%, Fig. 7D and F). These results indicate that the combination of complexes with ICIs can significantly improve the antitumor immune response. All the groups maintained stable body weights without significant differences (Fig. 7E), and HE staining shows that no serious structural or pathological alterations are observed in the major organs of mice in all treatment groups (Fig. S51), indicating that **Ir1** alone or in combination with BMS-1 has good biocompatibility.

Flow cytometry reveals an elevation in CD86+ CD80+ cells in the **Ir1** + BMS-1 treatment group (from about 1.77% to 10.8%; Fig. 7G), suggesting that the combination therapy promotes the maturation of DC cells. The impact of either cisplatin or BMS-1 on DC cells is not obvious. Furthermore, the treatment of **Ir1** + BMS-1 induces an increase in the percentage of CD8+ T cells, from 6.21% to 21.2% (Fig. 7H). Both **Ir1a** + BMS-1 and **Ir1** treatment groups show certain effects on DC cell maturation and CD8+ T cell infiltration.

Immunofluorescence (IF) staining shows that **Ir1**, **Ir1** + BMS-1, and **Ir1a** + BMS-1 treatment stimulates CD4/CD8 T cell infiltration into tumor tissues in primary and recurrent tumors, which is consistent with the results of flow cytometry (Fig. 8A–

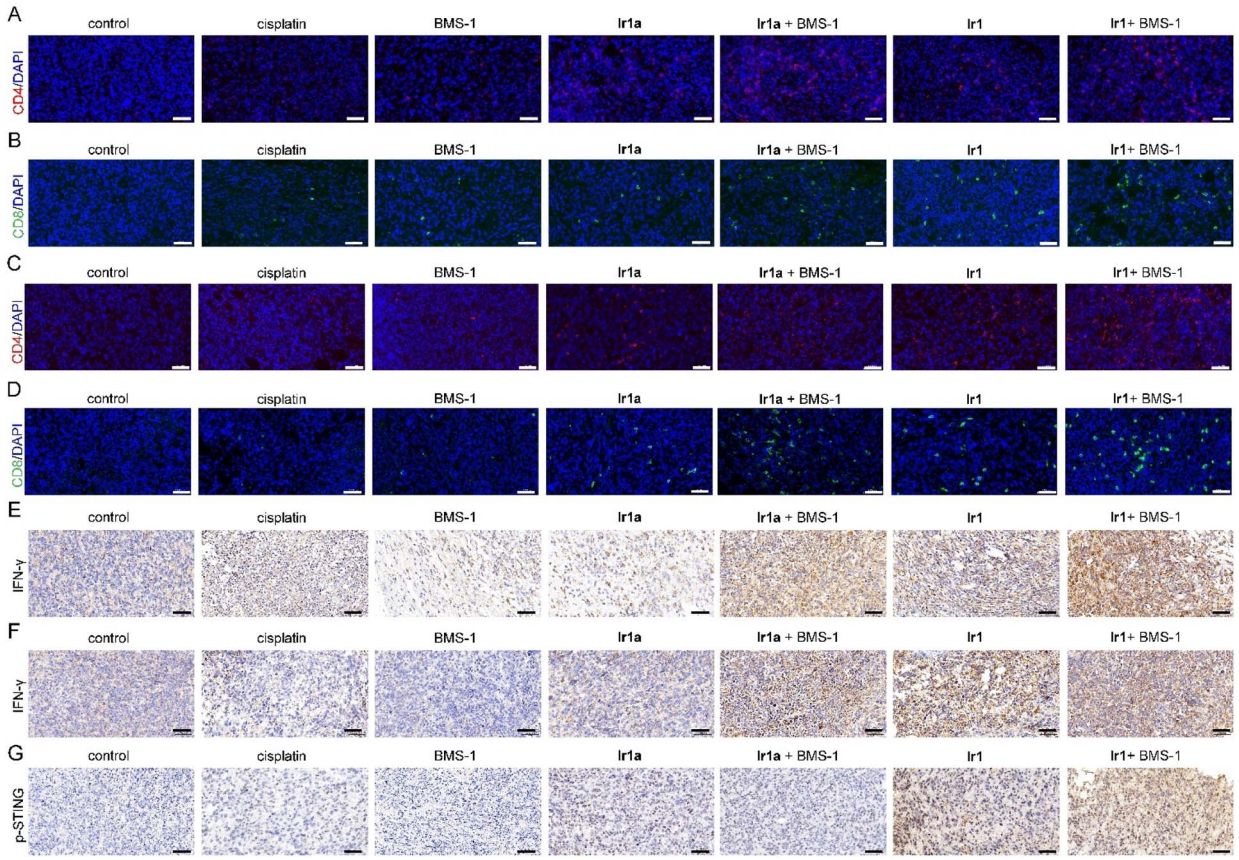

Fig. 8 (A and B) IF staining of recurrent tumor tissue for CD4 and CD8. (C and D) IF staining of primary tumor tissue for CD4 and CD8. (E) Expression of IFN-γ in recurrent tumor tissues. (F and G) Expression of protein in primary tumor tissues. Scale bar: 50 μm.

D). Immunohistochemistry (IHC) demonstrates that the combined treatment of metal complexes and BMS-1 increases the expression of interferon-γ (IFN-γ), one of the cytokines for tumor immune regulation (Fig. 8E and F). In addition, **Ir1** effectively elevates the expression of p-STING on primary tumors, whereas **Ir1a** or cisplatin can't activate the STING pathway *in vivo* (Fig. 8G). These results indicate that **Ir1** can effectively inhibit tumor growth and activate immune responses, and it further can synergistically act with immune checkpoint inhibitors to effectively improve the immune TMEs.

Conclusions

We have designed a series of iridium complexes that can sequester zinc in mitochondria. By utilizing the specific response phosphorescence lifetimes of **Ir1** to zinc and TPPLIM, we prove that **Ir1** can chelate zinc in mitochondria. Interestingly, the *in situ* formation of the heteronuclear complex **Ir1-Zn$_2$** exhibits nuclease-mimetic activity, enabling the degradation of mtDNA. This process facilitates the cytoplasmic release of mtDNA fragments to activate the cGAS-STING signaling pathway. As a consequence, **Ir1** can induce tumor cell necrosis by increasing mitochondrial ROS and breaking the zinc homeostasis. RNA-seq also proves that **Ir1** modulates intracellular zinc ion homeostasis and regulates cancer immune signaling pathways. *In vivo* experiments reveal that **Ir1** synergizes with ICIs to inhibit primary tumors and exert vaccine effects, thus improving the immune TMEs and inhibiting the growth of dismal tumors. By combining the mitochondria-targeting and imaging capabilities of Ir(III) complexes, we constructed the first phosphorescent metal complex capable of disrupting intracellular zinc homeostasis and generating a nuclease *in situ*, providing an efficient strategy to activate the cGAS-STING immune pathway.

Ethical statement

The animal experiment procedures were approved by the Institutional Animal Care and Use Committee of Sun Yat-sen University and performed in accordance with the ethical guidelines of Sun Yat-sen University. The accreditation number is SYSU-IACUC-2025-000460.

Author contributions

Zhi-Yuan Li: conceptualization, data curation, formal analysis, visualization, writing – original draft. Long-Bo Yu: data curation, formal analysis, visualization. Qing-Hua Shen: data curation, formal analysis, visualization. Liang Hao: formal analysis, funding acquisition, visualization. Peng Wang: data curation. Xiao-Xiao Chen: visualization. Yu-Yi Ling: conceptualization, data curation, formal analysis, visualization, writing – review & editing. Cai-Ping Tan: conceptualization, funding acquisition, project administration, writing – review & editing.

Conflicts of interest

There are no conflicts to declare.

Data availability

The data generated in this study are available within the article, supplementary information (SI), source data, and from corresponding authors upon request. Source data are provided in this paper. Supplementary information is available. See DOI: https://doi.org/10.1039/d5sc07181j.

Acknowledgements

This study was supported by the National Natural Science Foundation of China (No. 22177142 and 22207136), the Guangdong Basic and Applied Basic Research Foundation (No. 2024B1515040028) and the Fundamental Research Funds for the Central Universities.

References

1 H. Ishikawa and G. N. Barber, *Nature*, 2008, **455**, 674.
2 A. Ablasser, M. Goldeck, T. Cavlar, T. Deimling, G. Witte, I. Röhl, K.-P. Hopfner, J. Ludwig and V. Hornung, *Nature*, 2013, **498**, 380.
3 G. N. Barber, *Nat. Rev. Immunol.*, 2015, **15**, 760.
4 S.-R. Woo, L. Corrales and T. F. Gajewski, *Trends Immunol.*, 2015, **36**, 250.
5 N. Samson and A. Ablasser, *Nat. Cancer*, 2022, **3**, 1452.
6 K. R. B. Lanng, E. L. Lauridsen and M. R. Jakobsen, *Nat. Immunol.*, 2024, **25**, 1144.
7 C. Y. Ding, Z. L. Song, A. C. Shen, T. T. Chen and A. Zhang, *Acta Pharm. Sin. B*, 2020, **10**, 2272.
8 L. Corrales, L. H. Glickman, S. M. McWhirter, D. B. Kanne, K. E. Sivick, G. E. Katibah, S.-R. Woo, E. Lemmens, T. Banda, J. J. Leong, K. Metchette, T. W. Dubensky and T. F. Gajewski, *Cell Rep.*, 2015, **11**, 1018.
9 T. Benkovics, F. Peng, E. M. Phillips, C. An, R. S. Bade, C. K. Chung, Z. E. X. Dance, P. S. Fier, J. H. Forstater, Z. Liu, Z. Liu, P. E. Maligres, N. M. Marshall, N. Salehi Marzijarani, J. A. McIntosh, S. P. Miller, J. C. Moore, A. J. Neel, J. V. Obligacion, W. Pan, M. T. Pirnot, M. Poirier, M. Reibarkh, B. D. Sherry, Z. J. Song, L. Tan, B. W. H. Turnbull, D. Verma, J. H. Waldman, L. Wang, T. Wang, M. S. Winston and F. Xu, *J. Am. Chem. Soc.*, 2022, **144**, 5855.
10 W. Chang, M. D. Altman, C. A. Lesburg, S. A. Perera, J. A. Piesvaux, G. K. Schroeder, D. F. Wyss, S. Cemerski, Y. Chen, E. DiNunzio, A. M. Haidle, T. Ho, I. Kariv, I. Knemeyer, J. E. Kopinja, B. M. Lacey, J. Laskey, J. Lim, B. J. Long, Y. Ma, M. L. Maddess, B.-S. Pan, J. P. Presland, E. Spooner, D. Steinhuebel, Q. Truong, Z. Zhang, J. Fu, G. H. Addona, A. B. Northrup, E. Parmee, J. R. Tata, D. J. Bennett, J. N. Cumming, T. Siu and B. W. Trotter, *J. Med. Chem.*, 2022, **65**, 5675.

11 J. M. Ramanjulu, G. S. Pesiridis, J. Yang, N. Concha, R. Singhaus, S.-Y. Zhang, J.-L. Tran, P. Moore, S. Lehmann, H. C. Eberl, M. Muelbaier, J. L. Schneck, J. Clemens, M. Adam, J. Mehlmann, J. Romano, A. Morales, J. Kang, L. Leister, T. L. Graybill, A. K. Charnley, G. Ye, N. Nevins, K. Behnia, A. I. Wolf, V. Kasparcova, K. Nurse, L. Wang, A. C. Puhl, Y. Li, M. Klein, C. B. Hopson, J. Guss, M. Bantscheff, G. Bergamini, M. A. Reilly, Y. Lian, K. J. Duffy, J. Adams, K. P. Foley, P. J. Gough, R. W. Marquis, J. Smothers, A. Hoos and J. Bertin, *Nature*, 2018, **564**, 439.

12 Z. L. Song, X. Y. Wang, Y. Zhang, W. T. Gu, A. C. Shen, C. Y. Ding, H. Li, R. X. Xiao, M. Y. Geng, Z. Q. Xie and A. Zhang, *J. Med. Chem.*, 2021, **64**, 1649.

13 B.-S. Pan, S. A. Perera, J. A. Piesvaux, J. P. Presland, G. K. Schroeder, J. N. Cumming, B. W. Trotter, M. D. Altman, A. V. Buevich, B. Cash, S. Cemerski, W. Chang, Y. Chen, P. J. Dandliker, G. Feng, A. Haidle, T. Henderson, J. Jewell, I. Kariv, I. Knemeyer, J. Kopinja, B. M. Lacey, J. Laskey, C. A. Lesburg, R. Liang, B. J. Long, M. Lu, Y. Ma, E. C. Minnihan, G. O'Donnell, R. Otte, L. Price, L. Rakhilina, B. Sauvagnat, S. Sharma, S. Tyagarajan, H. Woo, D. F. Wyss, S. Xu, D. J. Bennett and G. H. Addona, *Science*, 2020, **369**, eaba6098.

14 E. N. Chin, C. Yu, V. F. Vartabedian, Y. Jia, M. Kumar, A. M. Gamo, W. Vernier, S. H. Ali, M. Kissai, D. C. Lazar, N. Nguyen, L. E. Pereira, B. Benish, A. K. Woods, S. B. Joseph, A. Chu, K. A. Johnson, P. N. Sander, F. Martínez-Peña, E. N. Hampton, T. S. Young, D. W. Wolan, A. K. Chatterjee, P. G. Schultz, H. M. Petrassi, J. R. Teijaro and L. L. Lairson, *Science*, 2020, **369**, 993.

15 J. Li, S. M. Canham, H. Wu, M. Henault, L. Chen, G. Liu, Y. Chen, G. Yu, H. R. Miller, V. Hornak, S. M. Brittain, G. A. Michaud, A. Tutter, W. Broom, M. E. Digan, S. M. McWhirter, K. E. Sivick, H. T. Pham, C. H. Chen, G. S. Tria, J. M. McKenna, M. Schirle, X. Mao, T. B. Nicholson, Y. Wang, J. L. Jenkins, R. K. Jain, J. A. Tallarico, S. J. Patel, L. Zheng, N. T. Ross, C. Y. Cho, X. Zhang, X.-C. Bai and Y. Feng, *Nat. Chem. Biol.*, 2023, **20**, 365.

16 X. J. Zhao, R. Zheng, B. B. Zhang, Y. Zhao, W. L. Xue, Y. Fang, Y. W. Huang and M. Z. Yin, *Angew. Chem., Int. Ed.*, 2024, **63**, e202318799.

17 S. X. Li, M. Luo, Z. H. Wang, Q. Feng, J. Wilhelm, X. Wang, W. Li, J. Wang, A. Cholka, Y.-X. Fu, B. D. Sumer, H. T. Yu and J. M. Gao, *Nat. Biomed. Eng.*, 2021, **5**, 455.

18 M. Luo, H. Wang, Z. H. Wang, H. C. Cai, Z. G. Lu, Y. Li, M. J. Du, G. Huang, C. S. Wang, X. Chen, M. R. Porembka, J. Lea, A. E. Frankel, Y.-X. Fu, Z. J. Chen and J. M. Gao, *Nat. Nanotechnol.*, 2017, **12**, 648.

19 Y. Jia, W. Jia, Z. Tang, Y. Wu, W. Yang, W. Ye, H. Ren, Y. Xie, Y. Chen and M. Yu, *Angew. Chem., Int. Ed.*, 2025, 202514516.

20 K. Shang, D. Tang, M. Cui, H. Hou, B. Xiao, J. Liu, R. Zhang, R. Kuai, J. Liu, H. Xiao, F. Huang and J. Wang, *Adv. Mater.*, 2025, 202506011.

21 P. Dosta, A. M. Cryer, M. Prado and N. Artzi, *Nat. Rev. Bioeng.*, 2025, **3**, 660.

22 Q. Yu, S. Sun, N. Yang, Z. Pei, Y. Chen, J. Nie, H. Lei, L. Wang, F. Gong and L. Cheng, *J. Am. Chem. Soc.*, 2025, **147**, 3161.

23 Q.-R. Li, X. Zhang, C. Zhang, Y. Zhang, M.-T. Niu, Z. Chen, S.-M. Zhang, J. He, W.-H. Chen and X.-Z. Zhang, *J. Am. Chem. Soc.*, 2025, **147**, 24555.

24 C. G. Wang, Y. K. Guan, M. Z. Lv, R. Zhang, Z. Y. Guo, X. M. Wei, X. X. Du, J. Yang, T. Li, Y. Wan, X. D. Su, X. J. Huang and Z. F. Jiang, *Immunity*, 2018, **48**, 675.

25 Y. Yang, H. H. Fan, X. Y. Xu, S. K. Yao, W. H. Yu and Z. J. Guo, *CCS Chem.*, 2024, **6**, 2210.

26 M. Du and Z. J. Chen, *Science*, 2018, **361**, 704.

27 Y.-Y. Ling, X.-Y. Xia, L. Hao, W.-J. Wang, H. Zhang, L.-Y. Liu, W. Liu, Z.-Y. Li, C.-P. Tan and Z.-W. Mao, *Angew. Chem., Int. Ed.*, 2022, **61**, e202210988.

28 S. R. Zhang, D. F. Song, W. H. Yu, J. Li, X. Y. Wang, Y. C. Li, Z. H. Zhao, Q. Xue, J. Zhao, J. P. Li and Z. J. Guo, *Natl. Sci. Rev.*, 2024, **11**, nwae020.

29 Y. Chen, S. Feng, L. Li, G. Liu, Q. Ma, Z. Liu, Y. Zhao and Q. Wang, *J. Med. Chem.*, 2025, **68**, 11928.

30 J.-Q. Wang, X.-M. Liu, Z.-S. Zhu, Z. Li, C.-Z. Xie, X. Qiao, Y.-K. Feng and J.-Y. Xu, *J. Med. Chem.*, 2025, **68**, 9661.

31 T.-Z. Ma, L.-Y. Liu, Y.-L. Zeng, K. Ding, H. Zhang, W. Liu, Q. Cao, W. Xia, X. Xiong, C. Wu and Z.-W. Mao, *Chem. Sci.*, 2024, **15**, 9756.

32 Y. Zheng, X.-X. Chen, D.-Y. Zhang, W.-J. Wang, K. Peng, Z.-Y. Li, Z.-W. Mao and C.-P. Tan, *Chem. Sci.*, 2023, **14**, 6890.

33 Y. L. Zeng, L. Y. Liu, T. Z. Ma, Y. Liu, B. Liu, W. Liu, Q. H. Shen, C. Wu and Z. W. Mao, *Angew. Chem., Int. Ed.*, 2024, **63**, e202410803.

34 Y. Li, B. Liu, Y. Zheng, M. Hu, L.-Y. Liu, C.-R. Li, W. Zhang, Y.-X. Lai and Z.-W. Mao, *J. Med. Chem.*, 2024, **67**, 16235.

35 Y.-Y. Ling, Z.-Y. Li, X. Mu, Y.-J. Kong, L. Hao, W.-J. Wang, Q.-H. Shen, Y.-B. Zhang and C.-P. Tan, *Eur. J. Med. Chem.*, 2024, **275**, 116638.

36 G. Xu, Q. Liang, L. Gao, S. Xu, W. Luo, Q. Wu, J. Li, Z. Zhang, H. Liang and F. Yang, *J. Med. Chem.*, 2024, **67**, 19573.

37 L. X. Cai, Y. Wang, Y. Y. Chen, H. H. Chen, T. Yang, S. R. Zhang, Z. J. Guo and X. Y. Wang, *Chem. Sci.*, 2023, **14**, 4375.

38 F. Li, Z. Wen, C. Wu, Z. Yang, Z. Wang, W. Diao, D. Chen, Z. Xu, Y. Lu and W. Liu, *J. Med. Chem.*, 2024, **67**, 1982.

39 X.-X. Chen, Z.-Y. Li, Q.-H. Shen, K. Peng, P. Wang, L.-B. Yu, Y.-Y. Han and C.-P. Tan, *ACS Nano*, 2025, **19**, 26953.

40 W. Qiao, J. Q. Chen, H. Y. Zhou, C. Hu, S. Dalangood, H. J. Li, D. D. Yang, Y. Yang and J. Gui, *Adv. Sci.*, 2024, **11**, 202305979.

41 Y. M. Xing, A. Peng, J. H. Yang, Z. F. Cheng, Y. Yue, F. L. Liu, F. H. Li, Y. Liu and Q. Liu, *Adv. Sci.*, 2024, **11**, 202309583.

42 L. Yi, X. Jiang, Z. G. Zhou, W. Xiong, F. Xue, Y. Liu, H. Z. Xu, B. Fan, Y. Li and J. L. Shen, *Adv. Mater.*, 2024, **36**, 202304328.

43 B. R. Kimmel, K. Arora, N. C. Chada, V. Bharti, A. J. Kwiatkowski, J. E. Finkelstein, A. Hanna, E. N. Arner, T. L. Sheehy, L. E. Pastora, J. Yang, H. M. Pagendarm, P. T. Stone, E. Hargrove-Wiley, B. C. Taylor, L. A. Hubert, B. M. Fingleton, K. N. Gibson-Corley, J. C. May,

J. A. McLean, J. C. Rathmell, A. Richmond, W. K. Rathmell, J. M. Balko and J. T. Wilson, *Nat. Biomed. Eng.*, 2025, **9**, 1719.
44 W. Maret, *Adv. Nutr.*, 2013, **4**, 82.
45 T. Kambe, T. Tsuji, A. Hashimoto and N. Itsumura, *Physiol. Rev.*, 2015, **95**, 749.
46 H. B. Fang, Y. H. Li, X. Z. Yang, Y. C. Chen, Z. J. Guo and W. J. He, *Curr. Opin. Chem. Biol.*, 2023, **76**, 102378.
47 E. Bafaro, Y. Liu, Y. Xu and R. E. Dempski, *Signal Transduction Targeted Ther.*, 2017, **2**, 17029.
48 A. K. Baltaci, K. Yuce and R. Mogulkoc, *Biol. Trace Elem. Res.*, 2017, **183**, 22.
49 B. Chen, P. Yu, W. N. Chan, F. Xie, Y. Zhang, L. Liang, K. T. Leung, K. W. Lo, J. Yu, G. M. K. Tse, W. Kang and K. F. To, *Signal Transduction Targeted Ther.*, 2024, **9**, 6.
50 J. Wang, H. H. Zhao, Z. L. Xu and X. X. Cheng, *Cancer Biol. Med.*, 2020, **17**, 612.
51 S. Alam and S. L. Kelleher, *Nutrients*, 2012, **4**, 875.
52 J. M. Goldberg and S. J. Lippard, *FEBS Lett.*, 2022, **597**, 151.
53 H. Woo, S. Cho, Y. Han, W.-S. Chae, D.-R. Ahn, Y. You and W. Nam, *J. Am. Chem. Soc.*, 2013, **135**, 4771.
54 Y. You, S. Cho and W. Nam, *Inorg. Chem.*, 2014, **53**, 1804.
55 S. Y. Ryu, M. Huh, Y. You and W. Nam, *Inorg. Chem.*, 2015, **54**, 9704.
56 K. Kikuchi, K. Komatsu and T. Nagano, *Curr. Opin. Chem. Biol.*, 2004, **8**, 182.
57 J. C. Shen, T. W. Rees, L. N. Ji and H. Chao, *Coord. Chem. Rev.*, 2021, **443**, 214016.
58 S. Pete, N. Roy, B. Kar and P. Paira, *Coord. Chem. Rev.*, 2022, **460**, 214462.
59 B. Kar, U. Das, N. Roy and P. Paira, *Coord. Chem. Rev.*, 2023, **474**, 214860.
60 Y. You, S. Lee, T. Kim, K. Ohkubo, W.-S. Chae, S. Fukuzumi, G.-J. Jhon, W. Nam and S. J. Lippard, *J. Am. Chem. Soc.*, 2011, **133**, 18328.
61 C. L. Zhang, M. S. Liu, S. X. Liu, H. Yang, Q. Zhao, Z. P. Liu and W. J. He, *Inorg. Chem.*, 2018, **57**, 10625.
62 R.-R. Ye, C.-P. Tan, L. He, M.-H. Chen, L.-N. Ji and Z.-W. Mao, *Chem. Commun.*, 2014, **50**, 10945.
63 F. Lafolet, S. Welter, Z. Popović and L. D. Cola, *J. Mater. Chem.*, 2005, **15**, 2820.
64 M. Bandini, M. Bianchi, G. Valenti, F. Piccinelli, F. Paolucci, M. Monari, A. Umani-Ronchi and M. Marcaccio, *Inorg. Chem.*, 2010, **49**, 1439.
65 X. Y. Yi, C. S. Zhang, S. Guo, J. Ma and J. Z. Zhao, *Dalton Trans.*, 2014, **43**, 1672.
66 P.-K. Lee, W. H.-T. Law, H.-W. Liu and K. K.-W. Lo, *Inorg. Chem.*, 2011, **50**, 8570.
67 H. A. Benesi and J. H. Hildebrand, *J. Am. Chem. Soc.*, 1949, **71**, 2703.
68 E. Tomat and S. J. Lippard, *Inorg. Chem.*, 2010, **49**, 9113.
69 D. Buccella, J. A. Horowitz and S. J. Lippard, *J. Am. Chem. Soc.*, 2011, **133**, 4101.
70 R. J. Radford, W. Chyan and S. J. Lippard, *Chem. Sci.*, 2014, **5**, 4512.
71 T. D. Rae, P. J. Schmidt, R. A. Pufahl, V. C. Culotta and T. V. O'Halloran, *Science*, 1999, **284**, 805.
72 F. Bulcke, R. Dringen and I. F. Scheiber, in *Neurotoxicity of Metals*, ed. M. Aschner and L. G. Costa, Springer International Publishing, Cham, 2017, pp. 313, DOI: 10.1007/978-3-319-60189-2_16.
73 W. Sun, M. Li, J.-L. Fan and X.-J. Peng, *Acc. Chem. Res.*, 2019, **52**, 2818.
74 Z. Liu, W. He and Z. Guo, *Chem. Soc. Rev.*, 2013, **42**, 1568.
75 Q. Zhao, F. Y. Li and C. H. Huang, *Chem. Soc. Rev.*, 2010, **39**, 3007.
76 C. Han, J. Jing, X. Zhao, J. Guo, S. Zheng and L. Du, *Biol. Trace Elem. Res.*, 2003, **94**, 113.
77 S. Mididoddi, J. P. McGuirt, M. A. Sens, J. H. Todd and D. A. Sens, *Toxicol. Lett.*, 1996, **85**, 17.
78 D. Desbouis, I. P. Troitsky, M. J. Belousoff, L. Spiccia and B. Graham, *Coord. Chem. Rev.*, 2012, **256**, 897.
79 T. Sarwar, S. U. Rehman, M. A. Husain, H. M. Ishqi and M. Tabish, *Int. J. Biol. Macromol.*, 2015, **73**, 9.
80 P. Kumar, S. Tomar, K. Kumar and S. Kumar, *Dalton Trans.*, 2023, **52**, 6961.
81 E. A. Schon, S. DiMauro and M. Hirano, *Nat. Rev. Genet.*, 2012, **13**, 878.
82 C. Bailly, *Life Sci.*, 2020, **246**, 117403.
83 J.-J. Lee, S. Y. Kim, S. H. Kim, S. Choi, B. Lee and J.-S. Shin, *Cell Death Dis.*, 2022, **13**, 791.
84 T. Yu, W. Nie, Z. Hong, Y. He, J. Chen, X. Mi, S. Yang, X. Li, B. Wang, Y. Lin and X. Gao, *Adv. Funct. Mater.*, 2021, **31**, 202100715.
85 J.-Y. Zhou, Q.-H. Shen, X.-J. Hong, W.-Y. Zhang, Q. Su, W.-G. Li, B. Cheng, C.-P. Tan and T. Wu, *Chem. Eng. J.*, 2023, **474**, 145516.
86 Q.-H. Shen, L.-B. Yu, S.-M. Yao, Z.-Y. Li, Q.-Q. Zhang, P. Wang and C.-P. Tan, *J. Med. Chem.*, 2025, **68**, 16284.